Journal of Materials Chemistry A

B-Terminated (111) Polar Surface of BP and BAs: Promising Metal-Free Electrocatalysts with Large Reaction Regions for Nitrogen Fixation

Journal:	*Journal of Materials Chemistry A*
Manuscript ID	TA-ART-02-2019-001410.R2
Article Type:	Paper
Date Submitted by the Author:	11-Apr-2019
Complete List of Authors:	Chen, Zhe; Harbin Normal University, Chemistry Zhao, Jing-Xiang; Harbin Normal University, Chemistry Yin, Lichang; Institute of Metal Research, Chinese Academy of Sciences Chen, Zhongfang; University of Puerto Rico, Department of Chemistry

SCHOLARONE™
Manuscripts

B-Terminated (111) Polar Surface of BP and BAs: Promising Metal-Free Electrocatalysts with Large Reaction Regions for Nitrogen Fixation

Zhe Chen,[a,b] Jingxiang Zhao,[a,*] Lichang Yin,[b,*] Zhongfang Chen[c,*]

[a] College of Chemistry and Chemical Engineering, and Key Laboratory of Photonic and Electronic Bandgap Materials, Ministry of Education, Harbin Normal University, Harbin, 150025, China

[b] Shenyang National Laboratory for Materials Science, Institute of Metal Research, Chinese Academy of Sciences, Shenyang, 110016, China

[c] Department of Chemistry, University of Puerto Rico, Rio Piedras Campus, San Juan, PR, 00931, USA

* To whom correspondence should be addressed. Email: xjz_hmily@163.com (JZ); lcyin@imr.ac.cn (LY); zhongfangchen@gmail.com (ZC)

ABSTRACT: The nitrogen electroreduction reaction (NRR) in aqueous solutions at ambient conditions represents an attractive prospect to produce ammonia, but the development of long-term stable and low-cost catalysts with high-efficiency and high-selectivity remains a great challenge. Herein, we investigated the potential of a new class of experimentally available boron-containing materials, *i.e.*, the cubic boron phosphide (BP) and boron arsenide (BAs), as metal-free NRR electrocatalysts by means of density functional theory (DFT) calculations. Our results revealed that gas phase N_2 can be sufficiently activated on the B-terminated (111) polar surface of BP and BAs, and effectively reduced to NH_3 via an enzymatic pathway with an extremely low limiting potential (-0.12 V on BP and -0.31 V on BAs, respectively). Especially, the two proposed B-terminated (111) surfaces not only have a large active region for N_2 reduction, but also can significantly inhibit the competitive hydrogen evolution reaction, thus have rather high efficiency and selectivity for NRR. Therefore, the cubic BP or BAs with mainly exposed (111) facets may serve as promising metal-free NRR catalysts with superior performance.

1. Introduction

Ammonia, one of the most important synthetic chemicals for human sustainable development, is not only a carbon-free energy carrier, but also of great significance to fertilizer production.[1-4] In industry, NH_3 has been routinely produced by the Haber-Bosch process for more than 100 years, in which gaseous N_2 and H_2 molecules are firstly dissociated into atomic N and H species, followed by their bonding into NH_3 on conventional Fe- or Ru-based catalysts. In this process, however, high temperature (about 300~500 °C) and high pressure (about 150~300 atm) are required to directly split the inert and strong N≡N bond.[5-7] In addition, this conventional NH_3 synthesis process consumes more than 1% of the global energy, and is accompanied by huge greenhouse gas emission.[8,9] Thus, it is highly desirable to develop alternative strategies for NH_3 synthesis.[10,11]

The electrochemical nitrogen reduction reaction (NRR) at ambient conditions is very attractive due to its much reduced energy input and favorable environmental compatibility,[12,13] in which electrocatalysts are the core components to reduce the reaction overpotential and increase the reaction rate and selectivity of N_2 reduction.[14,15] Currently, the transitional metals-based NRR electrocatalysts working at ambient conditions have been widely investigated both experimentally and theoretically, including metal nitrides and oxides, or single metal atoms anchored on various substrates.[16-23] However, the practical application of these metal-based NRR electrocatalysts has been severely limited by their low selectivity, high overpotential, easy deactivation, and detrimental environment impact.[9,13,24]

In recent years, the emerging metal-free catalysts for NRR have attracted increasing attention due to their intrinsic advantages, such as low cost, high reliability, good biocompatibility, and excellent sustainability. In particular, boron-based heterogeneous electrocatalysts have demonstrated their strong potentials to capture and convert N_2 molecules to NH_3 in aqueous solutions at ambient conditions based on the so-called "acceptance-donation" mechanism.[25,26] For example, Yu *et al.* experimentally confirmed that the boron-doped graphene with the doping level of 6.2% can achieve a NH_3 production rate of 9.8 $\mu g \cdot hr^{-1} \cdot cm^{-2}$ and faradic efficiency of 10.8% at −0.5 V versus reversible hydrogen electrode.[27] Ling *et al.* proposed that the B atom anchored on graphitic-carbon nitride ($g\text{-}C_3N_4$) could be utilized as a metal-free NRR photocatalyst under visible light drive with a record low onset potential (–0.20 V).[28] Qiu *et al.* revealed that boron carbide (B_4C) nanosheet could act as a metal-free catalyst for high-performance electrochemical nitrogen-to-ammonia fixation, which can achieve a high ammonia yield of 26.57 $\mu g\ h^{-1}\ mg^{-1}$ and a fairly high Faradaic efficiency of 15.95% at –0.75 V versus reversible hydrogen electrode.[29] Though significant progress has been made, it is still a big challenge for the development of high-efficient electrocatalysts with large reaction regions (or high concentration of B species), which could render its catalytic activity be fully achieved.

From this perspective, we intuitively speculate that the most common B-containing compounds in III-V semiconductors, such as cubic boron nitride (BN), boron phosphide (BP) and boron arsenide (BAs), may show possible NRR activity. Note that these cubic III-V semiconductors are experimentally available, and their

applications as high thermal conductivity materials have attracted great attentions. Moreover, cubic BP is a promising electronic material for harsh environmental application, due to its good stability at high temperatures, high mechanical hardness, modest band gap (2.00 eV), and high dielectric constant.[30,31] The recently synthesized high-purity cubic BAs[32] have similar electronic properties as Si[33] with a moderate band gap (1.50 eV),[34] thus are promising for applications in electronics and photovoltaics. However, cubic BN is not suitable for electroreduction application because of its extremely large band gap around 6 eV.[35]

Considering the high abundance of B species in cubic BP and BAs, an interesting question arises: can the experimentally available cubic BP and BAs be directly utilized as metal-free electrocatalysts for NRR? To address this question, in this work, by means of comprehensive density functional theory (DFT) computations, we explored the catalytic performance of their (100), (110), and (111) surfaces towards NRR. Our computations showed that among these three considered surfaces, the B-terminated (111) surface exhibits the highest NRR catalytic activity with a low limiting potential (-0.12 V for BP and -0.31 V for BAs, respectively) via an enzymatic reduction mechanism. Meanwhile, the hydrogen evolution side reaction can be significantly inhibited, suggesting the high selectivity towards NRR. Therefore, B-terminated (111) surfaces of cubic BP and BAs are quite promising metal-free electrocatalysts for NRR with large active region, high efficiency and selectivity, which opens a new door to advance the sustainable NH_3 production.

2. Computational Methods

Our spin-polarized DFT computations were performed using the Vienna Ab Initio Simulation Package (VASP) unless stated otherwise.[36] The exchange correlation energy was represented by the Perdew-Burke-Ernzerhof (PBE) functional within the generalized gradient approximation (GGA) and the electron-ion interactions were described by the projector augmented wave (PAW) method.[37-39] The (100), (110), and (111) surfaces of cubic BP and BAs were constructed to explore the possible NRR activity. All these surfaces consist of four BP/BAs atomic layers, which are thick enough for energy convergence based on the test calculations (Table S1). The bottom two BP/BAs atomic layers are fixed, while atoms in other layers are fully relaxed during geometry optimizations. A 4×4 supercell was used for the (100) and (111) surfaces, while a 3×4 supercell was employed for the (110) surface in order to obtain similar supercell size. Dipole correction was employed to correct potential spurious terms arising from the asymmetry of the slabs.[40] A Monkhorst-Pack *k*-point mesh of 3×3×1 was used to sample the Brillouin zone, and the plane-wave cut-off energy was set to be 500 eV. All the structures were fully relaxed until the forces on each atom (except for those fixed ones) were less than 0.03 eV/Å and the convergence criterion for the electronic structure iteration was set to be 10^{-5} eV. The van der Waals (vdW) interactions were described by using the empirical correction in Grimme's method (DFT+D3).[41] The vacuum space was set to be 20 Å in the *z* direction, which was large enough to minimize the interactions between periodic images. The climbing image nudged elastic band (CI-NEB) method was used to find saddle points and minimum-

energy paths.[42] Hirshfeld population analysis[43] was performed by PBE functional with DNP basis set using DMol^3 program.[44]

To investigate the thermodynamic stability of different surfaces under examination, we firstly calculated the surface energy (γ_s) following the definition $\gamma_s = \frac{1}{2A}\left(E_{surface}^{relax} - N_{atoms} \times E_{bulk}\right)$, where A is the surface area, $E_{surface}^{relax}$ is the energy of the relaxed surface, N_{atoms} is the number of atoms in the slab, and E_{bulk} is the bulk energy per atom. According to this definition, the surface with a smaller γ_s value has a higher thermodynamic stability and higher probability of natural exposure. To further evaluate the thermal stability of relevant surfaces, *ab initio* molecular dynamics (AIMD) simulations were performed in the canonical ensemble (NVT) with Nose-Hoover thermostat at 500K for a time period of 10 ps with a time step of 2 fs.[45,46]

The adsorption energies (E_{ads}) of the NRR intermediates were determined by $E_{ads} = E_{total} - E_{slab} - E_{ads\,orbate}$, where E_{total}, E_{slab} and $E_{ads\,orbate}$ represent the total energies of the species-adsorbed slab system, clean slab, and the adsorbate, respectively. According to this definition, a more negative adsorption energy indicates a stronger adsorption.

The Gibbs reaction free energy change (ΔG) of each elementary step in the NRR process was calculated by using the computational hydrogen electrode (CHE) model proposed by Nørskov *et al.*,[47] in which the chemical potential of the proton-electron pair in aqueous solution is equal to one-half of the chemical potential of a hydrogen molecule. Based on this model, the ΔG value can be obtained by $\Delta G = \Delta E + \Delta ZPE - T\Delta S + \Delta G_{pH} + eU$, where ΔE is the reaction energy of

reactant and product species adsorbed on catalyst surface directly obtained from DFT computations; ΔZPE and ΔS are the changes of zero point energies and entropies between the adsorbed species and the gas phase molecules at 298.15 K, which were calculated from the vibrational frequencies. ΔG_{pH} is the free energy correction of pH, which can be calculated by $\Delta G_{pH} = K_B T \times pH \times ln10$. Notably, the pH value was set to be zero in this work for simplicity; U was the applied potential.

3. Results and Discussions

3.1 Structures, stabilities and properties of B-terminated surfaces

Since the crystal structures of cubic BP and BAs are identical except for the lattice constants, the atomic structures of their corresponding low-index surfaces, such as (100), (110), and (111), are also be very similar. Thus, for simplicity, we chose BP as a representative when discussing the surface atomic structures, and Figure 1 presents the atomic structures of the optimized (100), (110), and (111) surfaces of cubic BP, while the detailed data for BAs are given in Figure S1 in the Supporting Information. Compared with the clean-cut surfaces, obvious surface reconstructions and relaxations occurred upon geometry optimization in order to reduce the surface energies or saturate the surface dangling bonds. In detail, for the BP (100) surface, two adjacent B atoms form B_2 dimers (bond length ca. 1.66 Å) to saturate the otherwise dangling bonds (Figure 1a), while the bond between surface B atom and its neighboring P atom is shortened to ca. 1.90 Å, which is slightly shorter than that (1.96 Å) in the bulk. In the case of BP (110) surface (Figure 1b), the surface B atoms take an obvious inward

relaxation, leading to a shortened B-P bond of ca. 1.92 Å. On the BP (111) surface (Figure 1c), the B and P atoms are located in slightly different planes: the B atoms are at the outermost layer, while the P atoms are at the inner layer, and the surface B-P bond length is ca. 1.89 Å due to the inward relaxation of surface B atoms. Note that almost the same surface reconstructions and/or relaxations can be observed for the (100), (110), and (111) surfaces of cubic BAs (Figure S1), and the surface relaxation behavior of cubic BP and BAs is very similar to cubic BN.[48-53]

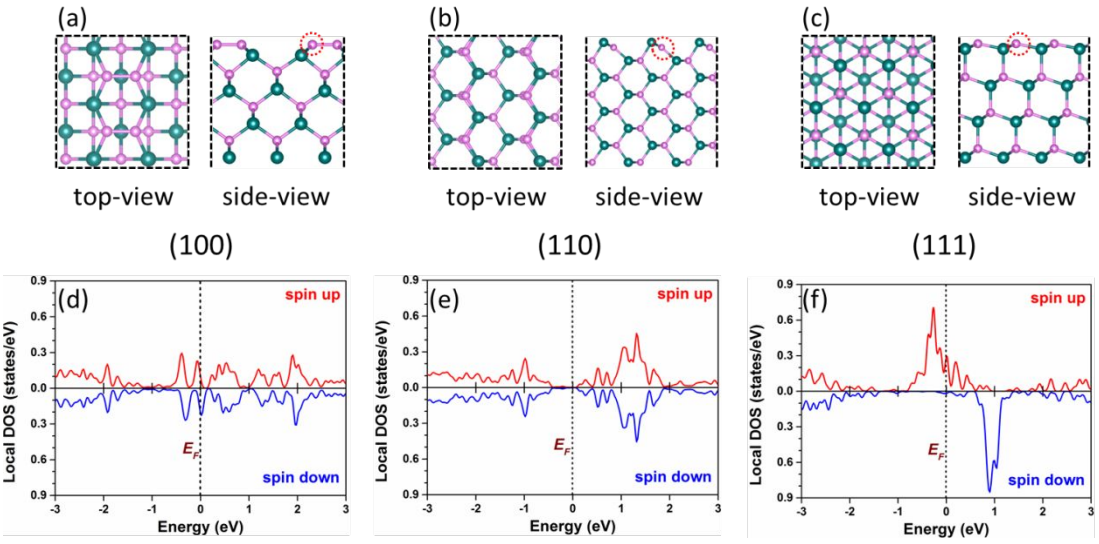

Figure 1. Schematic atomic structures of (a) the (100) surface, (b) the (110) surface, and (c) the (111) surface of cubic BP. The local density of states (LDOS) of surface B atoms marked by red dashed circle on (d) the (100) surface, (e) the (110) surface, and (f) the (111) surface of cubic BP. The Fermi level (E_F) was set to be zero and denoted by the black dashed line.

In order to identify which surface is more dominantly exposed for both cubic BP and BAs, we calculated the surface energies of these three low-index crystal surfaces. Our results revealed that B-terminated (100), (110), and (111) surfaces have similar surface energies for both BP and BAs, implying their similar thermodynamic stabilities

and almost the same possibilities to be exposed. In addition, we also explored the P- or As-terminated (100) and (111) surfaces. We found that the P/As-terminated surfaces generally have higher surface energies than B-terminated ones, suggesting that the B-terminated surfaces have higher thermodynamic stability and higher probability of natural exposure. Thus, we only focus on the NRR process on B-terminated surfaces in the following discussion.

Since electronic properties play an important role in the adsorption, activation, and subsequent reduction of N_2 on corresponding surfaces, we examined the local density of states (LDOS) of surface B atoms on the three considered low-index surfaces for both BP and BAs (Figure 1 and Figure S1). The (111) surfaces are greatly spin-polarized with rather high spin magnetic moments (7.92 and 7.84 μ_B for BP and BAs, respectively), which are mainly contributed from the surface B atoms (Figure S2). Note that previous studies revealed that the surface spin polarization facilitates the activation of N_2 molecule,[3,16,54,] thus, the surface B atoms on the (111) surfaces may also have potential to activate the inert N_2 molecule. On the contrary, the (100) and (110) surfaces of BP and BAs have almost no spin polarization due to the formation B-B dimer and the inward relaxation of surface B atoms, respectively. Note that the same polarization/non-polarization characteristics observed in the corresponding surfaces in BN.[53,55] Interestingly, the LDOS of BP (111) (Figure 1f) is obviously higher than those of BP (100) and BP (110) surfaces (Figure 1d and 1e) around the Fermi level. Similar results were also observed for cubic BAs (Figure S1d-f). Thus, the B atoms on the BP (111) and BAs (111) surfaces may accumulate more electrons around the Fermi level,

which could be easily transferred into the anti-bonding orbitals of N_2, facilitating to activate the inert N_2 molecule. Meanwhile, each B atom on the (111) surfaces forms three covalent bonds with neighboring P or As atoms, leaving one empty orbital to accept the lone pairs electrons of N_2 molecule, which is very similar to the proposed "acceptance-donation" process observed in B-decorated g-C_3N_4 nanosheet.[28] All these analyses suggest that the (111) surfaces may possess higher chemical activity toward N_2 molecule than (110) and (100) surfaces, which will be further discussed in the following sections.

3.2. Adsorption of N_2 on B-terminated surfaces

The adsorption of N_2 on the catalyst surface is the first step for the NRR pathway, which is crucial for the subsequent reaction steps. Two different adsorption configurations, including end-on and side-on patterns, were considered for N_2 adsorption on all the relevant surfaces of BP (Figure 2) and BAs (Figure S3). After fully structural relaxation, the calculated N_2 adsorption energies are summarized in Table 1, while the corresponding free energies are given in Table S3.

Table 1. The calculated adsorption energies (eV) of N_2 molecule with side-on and end-on patterns on the (100), (110) and (111) surfaces of BP and BAs.

configuration	BP			BAs		
	(100)	(110)	(111)	(100)	(110)	(111)
side-on	-0.19	-0.12	-0.53	-0.07	-0.11	-0.56
end-on	-0.54	-0.44	-0.64	-0.55	-0.68	-0.76

For simplicity, we took the (111) surface of BP as a representative to describe N_2 adsorption behavior. The adsorption energies of N_2 molecule on BP (111) surface are -0.53 and -0.64 eV for the side-on and the end-on patterns, respectively. Thus, the end-on pattern is more favorable thermodynamically than side-on one. Furthermore, the newly formed B-N bond lengths are ca. 1.47 Å (end-on) and 1.62 Å (side-on), respectively (Figure 2c and 2d), which are shorter than that of BH_3NH_3 (1.65 Å), indicating a strong adsorption of N_2 molecule on the (111) surface. Due to this strong adsorption, the B atoms adsorbed by N_2 extrude from the original plane by ca. 0.21 Å (side-on) and 0.16 Å (end-on), respectively.

Remarkably, the N≡N bond is elongated from 1.12 Å in a free N_2 molecule to 1.24 Å upon adsorption via the side-on manner. For comparison, for the end-on case, the N≡N bond of the adsorbed N_2 molecule is only slightly elongated to 1.13 Å. The difference in the N_2 bond elongation can be well understood by the different amount of charge transfer from the substrate to the N_2 molecule. According to Hirshfeld population analysis, the charge transfer (0.16 electrons) in the side-on pattern is more significant than that (0.05 electrons) in the end-on case, which leads to the obvious elongation of the N-N bond in the side-on pattern. Note that similar bond elongation occurs for N_2 molecule on BAs (111) surface (Figure S3).

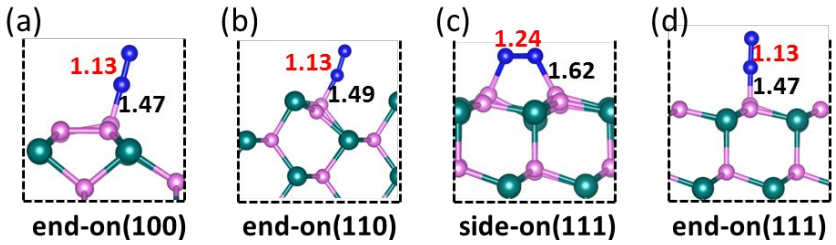

Figure 2. Schematic diagram of all stable nitrogen adsorption configurations in (a) the (100) surface, (b) the (110) surface, (c) and (d) the (111) surface of BP, in which the red value is N-N bond length, and the black value is B-N bond length (Å).

To get a deeper insight into the observed N_2 activation on BP (111) surface, we further examined the charge density difference of N_2 adsorbed on BP (111) (Figure 3) and BAs (111) surfaces (Figure S4). Interestingly, the charge transfer is a "two-way" process, and N_2 adsorption follows the "acceptance-donation" process:[28] the charge accumulation and depletion can be observed for both N_2 molecule and terminated B atoms, in which B atoms accept the lone-pair electrons and simultaneously donate electrons to the anti-bonding orbitals of N_2. Such an "acceptance-donation" process can be further confirmed by comparing the LDOS of BP (111) and BAs (111) surfaces before and after N_2 adsorption (Figure S5), for both BP (111) and BAs (111) surfaces, the LDOS of surface B atoms clearly decrease and the spin polarization has been significantly quenched after N_2 adsorption with the side-on pattern (Figure S2). Overall, the above results reveal that the inert N_2 molecule can be sufficiently activated on BP (111) and BAs (111) surfaces, which would facilitate its subsequent reduction reactions.

In addition, we also explored N_2 adsorption behavior on the (100) and (110) surfaces. For these two surfaces, N_2 molecule prefers to be adsorbed via the end-on

pattern (Figure 2a and 2b) with the adsorption energies ranging from -0.44 to -0.68 eV, while only weak adsorption is observed for side-on pattern with adsorption energies ranging from -0.07 to -0.19 eV (Table 1). Thus, in the following sections, only the end-on pattern of N_2 molecule on (100) and (110) surfaces was focused for its further reduction.

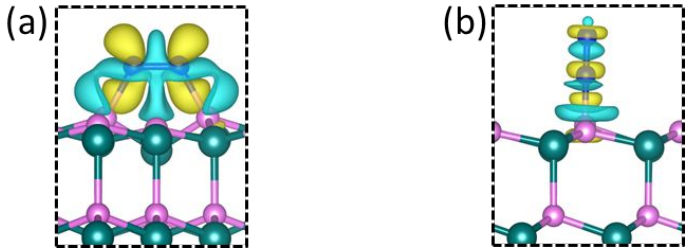

Figure 3. Difference charge density of BP (111) surface with the adsorption of N_2 via (a) side-on pattern and (b) end-on pattern, where the isosurface value is set to be 0.005 e Å^{-3} and cyan and yellow regions represent positive and negative charges, respectively.

3.3. Reaction mechanism and free energy for NRR

The NRR process involves six net coupled proton and electron transfer steps, which can be simply written as: $N_2(g) + 6H^+ + 6e^- \rightarrow 2NH_3$. During the NRR process, N_2 molecule is gradually hydrogenated by the protons from the solution and electrons from electrode, producing various N_xH_y intermediates, including N_2H^*, $N_2H_2^*$, $N_2H_3^*$, $N_2H_4^*$, N^*, NH^*, and NH_2^*. As well understood, the N_2 molecule can be reduced to NH_3 through three reaction pathways, namely, enzymatic, distal, and alternating pathways.[9,23,28] In general, the side-on adsorbed N_2 can be reduced to NH_3 through enzymatic mechanism, in which its two N atoms are hydrogenated alternately, and the second NH_3 will be generated immediately after the first one is released. For the end-on adsorption configuration, the NRR proceeds following either the distal or the

alternating pathway. In the distal pathway, the remote N atom is firstly hydrogenated to release NH_3, while the two N atoms will be hydrogenated simultaneously in the alternating pathway. To evaluate the NRR catalytic activity, we computed the free energy changes (ΔG) of each elementary step in the NRR via the enzymatic, distal, and alternating mechanisms.

The computed Gibbs free energy diagrams of NRR on the (111) surfaces of BP and BAs along the enzymatic pathway were presented in Figure 4a and 4b, together with the corresponding adsorbed species structures. The free energy diagrams of distal and alternating pathway listed in Figure S6 (BP) and Figure S7 (BAs) with the corresponding structures of the reaction intermediates. Notably, for the computations of free energies of each elementary step in the NRR, the involved vibrational frequencies, zero point energies, and entropic corrections of all intermediates were summarized in Table S4.

Following the enzymatic pathway, on BP (111) surface, the activated N_2 molecule with side-on pattern will be firstly hydrogenated to N_2H^* species with the ΔG value of -0.44 eV. Subsequently, the formed N_2H^* species is further reduced to be $NHNH^*$, $NHNH_2^*$, NH_2^*+NH_2^*, NH_2^* and NH_3^*. In this case, all the elementary steps are downhill in the free energy profiles, except for the formation of the second NH_3 ($NH_2^* + H^+ + e^- \rightarrow NH_3^*$) with the ΔG value of +0.12 eV (Figure 4a). Thus, this step is the potential-determining step (PDS) for the whole NRR with a rather low limiting potential (-0.12 V). Remarkably, the direct desorption of the formed NH_3 from BP or BAs surface could be difficult due to its large free energies (1.20 ~ 1.60 eV). However,

the NH_3 desorption is not a problematic obstacle due to the following reasons: 1) the released energy (about 3.40 eV, Figure 4) at the corresponding hydrogenation steps is large enough to overcome the required energy for the release of the formed NH_3 (1.20~1.60 eV);[28, 29] 2) the formed NH_3^* can be hydrogenated into NH_4^+ under strongly acidic conditions, which has been observed in previous reports on the electrochemical reduction of nitric oxide.[56]

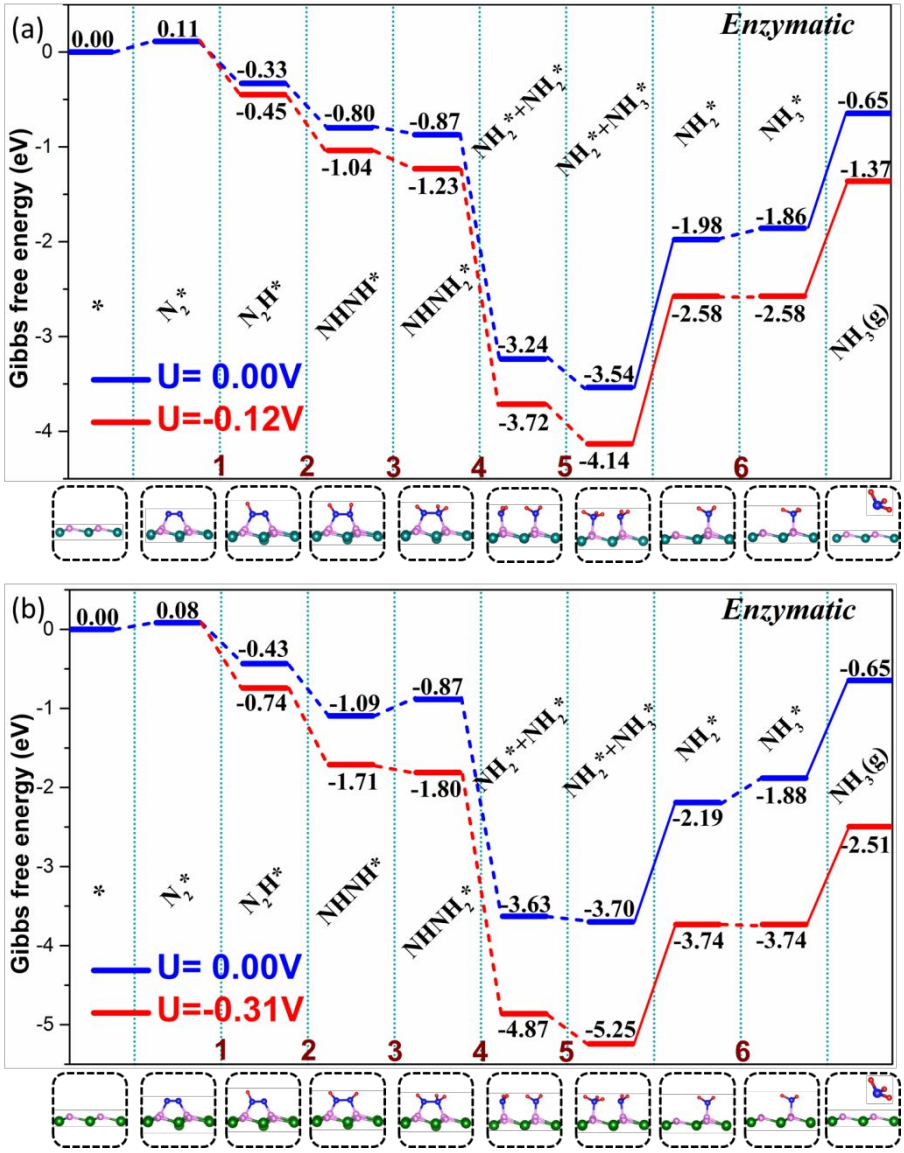

Figure 4. Gibbs free energy diagrams for N_2 reduction through enzymatic mechanisms on (a) BP (111) surface and (b) BAs (111) surface at applied potentials, together with the corresponding adsorbed species structures.

When the NRR proceeds through the distal or alternating pathway (Figure S6), the potential-determining step locates at the formation of the first NH_3 or the N_2H^* species due to the maximum ΔG value (0.99 or 0.49 eV), which is much higher than that of

enzymatic pathway (0.12 eV), suggesting that the nitrogen reduction on BP (111) surface prefers to take place through the enzymatic pathway. Similarly, on BAs (111) surface, the enzymatic pathway is also the most favorable for the NRR (Figure 4b), and the reaction step of $NH_2^* \rightarrow NH_3^*$ is the PDS with the free energy change of 0.31 eV, which is about two times higher than that of BP (0.12 eV).

Notably, though the side-on pattern is slightly less favorable than the end-on pattern for the N_2 adsorption on the (111) surfaces, the free energies of the formed N_2H^* species in the side-on pattern in the enzymatic pathway is more stable by about 0.84 eV (BP) and 0.81 eV (BAs) than that in the end-on pattern. The activation barrier for N_2H^* to transfer from the end-on to side-on pattern is rather small (0.02 eV for BP, 0.01 eV for BAs) (for details, see Figure S8 in the Supporting Information).

Thus, we also considered the mixed catalytic pathway, *i.e.*, N_2 is firstly adsorbed on catalyst surface in the end-on pattern, followed by its hydrogenation to N_2H^* species with a side-on pattern, and the subsequent elementary steps follow the enzymatic pathway (Figure S9 in Supporting Information). Note that in the actual reactions, this mixed pathway is most favorable. Since the PDS is the formation of the second NH_3, the limiting potential in this preferred mixed catalytic pathway is the same as the enzymatic pathway (-0.12 V).

In addition, we explored the catalytic performance of (100) and (110) surfaces of BP and BAs. Since only the end-on pattern is stable for N_2 adsorption on these surfaces, the NRR prefers to occur through the distal or the alternating pathway. We first studied the hydrogenation of the adsorbed N_2 molecule to N_2H^* species, and found that the free

energy of N_2H^* formation on the (100) and (110) surfaces of BP or BAs is at least 0.66 eV, which is much larger than that of the corresponding (111) surfaces (0.12 eV for BP and 0.31 eV for BAs). Thus, the NRR activity of the (100)/(110) surfaces of BP and BAs is much lower than the corresponding (111) surfaces, and will not further studied.

Our above studies revealed that the BP (111) surface exhibits the highest catalytic activity towards NRR among all the considered surfaces, its limiting potential (-0.12 V) is even lower than that of the recently reported B-decorated g-C_3N_4 with a record low limiting potential (-0.20 V).[28]

3.4. Stability against poisoning

The hydrogen evolution reaction (HER) is a one of competing electrochemical reaction against NRR, since the adsorbed H could block the effective active sites and thus reduce the Faraday efficiency. For the HER, due to the strong interaction between H and B atoms, the HER process is hindered by the Heyrovskey step ($H^* + H^+ + e^- \rightarrow H_2$) with the computed free energy barriers of 1.38 and 1.52 eV, respectively, which are much larger than that of NRR (0.12 and 0.31 eV, Figure 4) suggesting that BP and BAs (111) surfaces exhibit outstanding catalytic performance for the NRR than HER.

In addition, we also compared the difference in the adsorption strength between H^* and N_2H^* species, because the formation of N_2H^* species is the first hydrogenation step and its adsorption strength on catalyst surfaces usually determinates the overpotential requirement on catalysts. Thus, a promising NRR catalyst should be able to stabilize N_2H speices.[57,58]

Note that the electrochemical ammonia synthesis usually involves associative or dissociative pathways.[57,58] In both pathways, two hydrogenation mechanisms exist: 1) Tafel-type mechanism,[59] in which the solvated protons from the solution first cover the catalyst surface and couple with electrons. Subsequently, the hydrogen adatoms react with N_2H_x or NH_x to yield NH_3. Notably, this mechanism is very slow at room temperature because the activation barriers for $H^* + NH_x^* \rightarrow NH_{x+1}^*$ reactions are generally larger than 1.00 eV. In particular, an applied bias can indirectly affect the thermochemical barrier by varying the concentrations of the reactants.[60,61] 2) Heyrovsky-type mechanism,[62] in which the adsorbed N_2H_x or NH_x species will be hydrogenated by direct attachment of protons from the solution and electrons from the electrode, and the applied bias has an direct influence on the energy barrier. In this study, the Heyrovsky-type mechanism was considered for the ammonia synthesis from NRR at room temperature, and the same assumptions have been widely employed in the electrochemical reaction of CO_2 and O_2.[63,64] The computed adsorption energies of N_2H^* in the side-on pattern are -3.38 eV (BP) and -3.49 eV (BAs), respectively, much more negative than that of H^* (-1.69 and -1.83 eV, respectively). Therefore, the N_2H^* species is energetically favorable to be adsorbed on the electrocatalysts rather than H species, and the hydrogen poisoning is not a big concern.

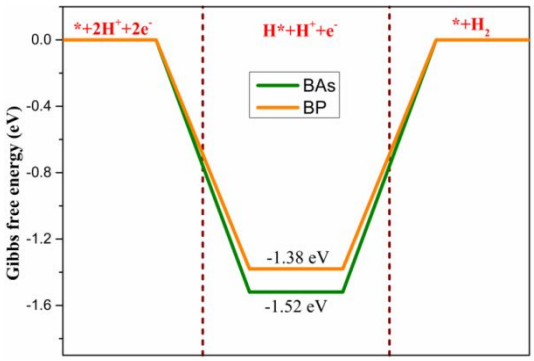

Figure 5. Gibbs free energy diagrams of HER on BP and BAs (111) surfaces.

Clearly, the (111) surfaces of BP and BAs possess an extremely excellent catalytic activity and selectivity for NRR. However, are these two surfaces stable at ambient conditions? To address this question, we performed AIMD simulations at 500K for 10ps with a time step of 2fs. Taking BP (111) surface as an example (Figure 6), the temperature and energy oscillate near the equilibrium state. The atomic structure of BP (111) surface remains intact without any obvious structure distortion during the AIMD simulation period, indicating its high stability of BP (111) surfaces. Such a high stability is also observed for the BAs (111) surface (Figure S10). With high stability at 500 K as demonstrated by AIMD simulations, we believe that the (111) surfaces of BP and BAs can be utilized as the highly efficient NRR electrocatalyst at ambient conditions (300 K).

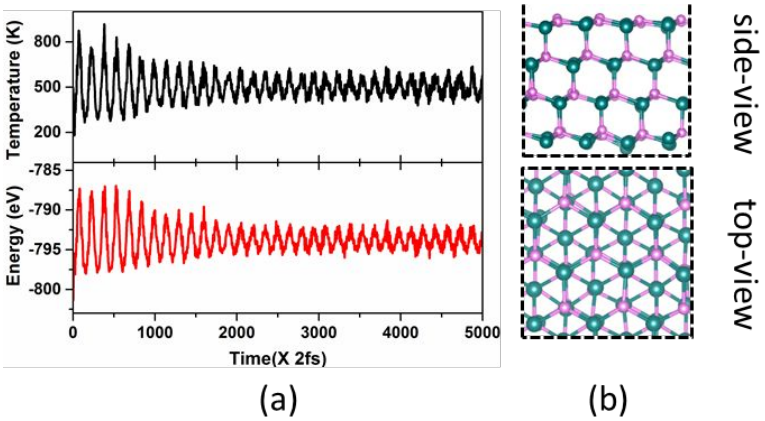

Figure 6. (a) Variations of temperature and energy against the time for AIMD simulations of BP, the simulation is run under 500K for 10 ps with a time step of 2 fs. (b) Schematic diagram of the structure after dynamics simulation.

Since the NRR generally proceeds under the aqueous solution, the proposed B-terminated (111) surfaces in our work could interact with the environmental water. Thus, we also considered the adsorption of H_2O molecule on BP and BAs (111) surfaces to evaluate their stability in practical applications. Our results demonstrated that H_2O could be adsorbed on the two catalyst surfaces with the adsorption energy of -0.95 eV, which is slightly negative than that of N_2 molecule (about -0.76 eV), indicating that the B-terminated catalysts prefer to be covered by H_2O. However, the adsorbed H_2O would easily react with free N_2 molecule with the help of proton and electron to form N_2H species (*i.e.*, $H_2O^* + N_2 + H^+ + e^- \rightarrow N_2H^* + H_2O$) with the free energy of -0.06 eV on BP (111) and -0.16 eV on BAs (111) surfaces, as N_2H^* species exhibits much stronger adsorption strength (about -3.40 eV) on the two catalysts than H_2O (-0.95 eV). Thus, the catalytic performance of the two B-terminated catalysts can be well preserved in the aqueous solution, which has been observed in recent experimental study.[65] Remarkably,

the ionic liquids that have high N_2 solubility was recently adopted to replace water as the electrolytes to achieve high conversion efficiency for N_2 electroreduction to ammonia under ambient conditions, which could suppress the unwanted HER and H_2O poisoning effects.[66]

Finally, we investigated the interaction between our newly proposed catalysts with O_2. Similar to the well-known black phosphorene[67,68] and silicene,[69] the two proposed B-terminated surfaces also exhibit high chemical reactivity towards O_2 molecule, leading to the formation of oxide units. Thus, chemisorption-induced oxidation will be a major cause for the degradation of BP and BAs catalysts. A promising solution to avoid the problematic oxidation is to develop passivation and encapsulation by an inert material, in the same way as we used BN,[70] polymethyl methacrylate (PMMA),[71] and alumina or AlO_x,[72,73] to protect the otherwise unstable phosphorene and silicene. Among these encapsulation techniques, AlO_x encapsulation using atomic layer deposition is probably the most appealing in terms of industrial application and scalability, which can make the encapsulated phosphorene stable for more than 2 weeks and resist more than 5,000 bending cycles.[72,73] On the other hand, the whole NRR process could be performed under oxygen-free conditions, as Wang and coworkers recently demonstrated in their experiments using black phosphorus nanosheets to selectively catalyze NRR under ambient conditions.[74] Overall, though BP and BAs could be unstable in air, we strongly believe that their superior NRR catalytic performance can be achieved in the quite near future by encapsulation techniques or under oxygen-free conditions. We also hope that our theoretical studies could inspire

experimental studies to explore the potentials of B-terminated surfaces for NRR and other important reactions.

4. Conclusions

In this work, we explored the NRR properties of the (100), (110), and (111) surfaces of cubic BP and BAs by DFT calculations. Our computations revealed that the (111) surfaces have comparable surface energies with those of (100) and (110) surfaces, and are stable at ambient conditions. Among all the considered surfaces, the (111) surfaces of BP and BAs exhibit superior catalytic performance for NRR due to their rather low limiting potential (-0.12 and -0.31 V for BP and BAs, respectively) and strong ability to inhibit hydrogen evolution reactions. Therefore, the cubic BP and BAs with mainly exposed (111) surfaces are a new class of metal-free low-cost electrocatalyst with large active region for N_2 reduction, and can be utilized as highly efficient electrocatalyst for sustainable NH_3 production.

Acknowledgement

This work was financially supported in China by the National Science Fund of China (No. 51472249), the Natural Science Funds for Distinguished Young Scholar of Heilongjiang Province (No. JC2018004), and the Excellent Young Foundation of Harbin Normal University (Grant No. XKYQ201304), and in USA by NSF-CREST Center for Innovation, Research and Education in Environmental Nanotechnology (CIRE2N) (Grant Number HRD-1736093). Most computations were performed on TianHe-1(A) at National Supercomputer Center in Tianjin, and a portion of this

research used computational resources at the Center for Nanophase Materials Sciences, which is a DOE Office of Science User Facility.

References

1. H. Hirakawa, M. Hashimoto, Y. Shiraishi and T. Hirai, *J. Am. Chem. Soc.* 2017, **139**, 10929-10936.
2. H. Li, J. Shang, Z. Ai and L. Zhang, *J. Am. Chem. Soc.* 2015, **137**, 6393-6399.
3. X.-F. Li, Q.-K. Li, J. Cheng, L. Liu, Q. Yan, Y. Wu, X.-H. Zhang, Z.-Y. Wang, Q. Qiu and Y. Luo, *J. Am. Chem. Soc.* 2016, **138**, 8706-8709.
4. S. Licht, B. Cui, B. Wang, F.-F. Li, J. Lau and S. Liu, *Science.* 2014, **345**, 637-640.
5. M. Kitano, Y. Inoue, Y. Yamazaki, F. Hayashi, S. Kanbara, S. Matsuishi, T. Yokoyama, S.-W. Kim, M. Hara and H. Hosono, *Nat. Chem.* 2012, **4**, 934.
6. M.A. van Kessel, D.R. Speth, M. Albertsen, P.H. Nielsen, H.J.O. den Camp, B. Kartal, M.S. Jetten and S. Lücker, *Nature.* 2015, **528**, 555.
7. S.J. Li, D. Bao, M.M. Shi, B.R. Wulan, J.M. Yan and Q. Jiang, *Adv. Mater.* 2017, **29**, 1700001.
8. M. Kitano, S. Kanbara, Y. Inoue, N. Kuganathan, P.V. Sushko, T. Yokoyama, M. Hara and H. Hosono, *Nat. Commun.* 2015, **6**, 6731.
9. X. Cui, C. Tang and Q. Zhang, *Adv. Energy Mater.* 2018, **8**, 1800369.
10. T. Spatzal, M. Aksoyoglu, L. Zhang, S.L. Andrade, E. Schleicher, S. Weber, D.C. Rees and O. Einsle, *Science.* 2011, **334**, 940-940.

11. L.M. Azofra, N. Li, D.R. MacFarlane and C. Sun, *Energ. Environ. Sci.* 2016, **9**, 2545-2549.

12. L. Zhang, Z.J. Zhao and J. Gong, *Angew. Chem. Int. Ed.* 2017, **56**, 11326-11353.

13. M. Li, H. Huang, J. Low, C. Gao, R. Long and Y. Xiong, *Small Methods*. 2018, **2**, 1800388.

14. Y. Liu, Y. Su, X. Quan, X. Fan, S. Chen, H. Yu, H. Zhao, Y. Zhang and J. Zhao, *ACS Catal.* 2018, **8**,1186-1191.

15. Q. Qin, T. Heil, M. Antonietti and M. Oschatz, *Small Methods*. 2018, **2**, 1800202.

16. Z. Wei, Y. Zhang, S. Wang, C. Wang and J. Ma, *J. Mater. Chem. A*. 2018, **6**, 13790-13796.

17. X. Wang, W. Wang, M. Qiao, G. Wu, W. Chen, T. Yuan, Q. Xu, M. Chen, Y. Zhang, X. Wang, J. Wang, J. Ge, X. Hong, Y. Li, Y. Wu and Y. Li, *Science Bulletin.* 2018, **63**, 1246-1253.

18. M. Nazemi, S.R. Panikkanvalappil and M.A. El-Sayed, *Nano Energy.* 2018, **49**, 316-323.

19. S. Hu, X. Qu, J. Bai, P. Li, Q. Li, F. Wang and L. Song, *ACS Sustain. Chem. & Engin.* 2017, **5**, 6863-6872.

20. Á.B. Höskuldsson, Y. Abghoui, A.B. Gunnarsdóttir and E. Skúlason, *ACS Sustain. Chem. & Engin.* 2017, **5**, 10327-10333.

21. E. Skulason, T. Bligaard, S. Gudmundsdóttir, F. Studt, J. Rossmeisl, F. Abild-Pedersen, T. Vegge, H. Jónsson and J.K. Nørskov, *Phys. Chem. Chem. Phys.* 2012, **14**, 1235-1245.

22. J. Wang, L. Yu, L. Hu, G. Chen, H. Xin and X. Feng, *Nat. Commun.* 2018, **9**, 1795.

23. Z. Chen, J. Zhao, C.R. Cabrera and Z. Chen, *Small Methods*. 2018, **2**, 1800368.

24. K. Ithisuphalap, H. Zhang, L. Guo, Q. Yang, H. Yang and G. Wu, *Small Methods.* 2018, **2**, 1800352.

25. M.-A. Légaré, G. Bélanger-Chabot, R.D. Dewhurst, E. Welz, I. Krummenacher, B. Engels and H. Braunschweig, *Science.* 2018, **359**, 896-900.

26. D.L. Broere and P.L. Holland, *Science.* 2018, **359**, 871-871.

27. X. Yu, P. Han, Z. Wei, L. Huang, Z. Gu, S. Peng, J. Ma and G. Zheng, *Joule*. 2018, **2**, 1610-1622.

28. C. Ling, X. Niu, Q. Li, A. Du and J. Wang, *J. Am. Chem. Soc.* 2018, **140**, 14161-14168.

29. W. Qiu, X.-Y. Xie, J. Qiu, W.-H. Fang, R. Liang, X. Ren, X. Ji, G. Cui, A.M. Asiri and G. Cui, *Nat. Commun*. 2018, **9**, 3485.

30. Q. Zheng, S. Li, C. Li, Y. Lv, X. Liu, P.Y. Huang, D.A. Broido, B. Lv and D.G. Cahill, *Adv. Funct. Mater*. 2018, **28**, 1805116.

31. L. Shi, P. Li, W. Zhou, T. Wang, K. Chang, H. Zhang, T. Kako, G. Liu and J. Ye, *Nano Energy*. 2016, **28**, 158-163.

32. J.S. Kang, M. Li, H. Wu, H. Nguyen and Y. Hu, *Science*. 2018, **361**, 575-578.

33. S. Chae, K. Mengle, J.T. Heron and E. Kioupakis, *Appl. Phys. Lett.* 2018, **113**, 212101.

34. T.-H. Liu, B. Song, L. Meroueh, Z. Ding, Q. Song, J. Zhou and M. Li, G. Chen, *Phys. Rev. B.* 2018, **98**, 081203.

35. N. Izyumskaya, D.O. Demchenko, S. Das, Ü. Özgür, V. Avrutin and H. Morkoç, *Adv. Electronic Mater.* 2017, **3**, 1600485.

36. G. Kresse, *Phys. Rev. B*. 1996, **54**,11169.

37. J.P. Perdew, J.A. Chevary, S.H. Vosko, K.A. Jackson, M.R. Pederson, D.J. Singh and C. Fiolhais, *Phys. Rev. B.* 1992, **46**, 6671.

38. P.E. Blöchl, *Phys. Rev. B.* 1994, **50**, 17953.

39. J.P. Perdew and Y. Wang, *Phys. Rev. B.* 1992, **45**,13244.

40. J. Neugebauer and M. Scheffler, *Phys. Rev. B.* 1992, **46**, 16067.

41. S. Grimme, *J. Comput. Chem.* 2006, **27**, 1787-1799.

42. G. Henkelman, B.P. Uberuaga and H. Jónsson, *J. Chem. Phys.* 2000, **113**, 9901-9904.

43. F.L. Hirshfeld, *Theore. Chim. Acta.* 1977, **44**, 129-138.

44. B. Delley, *J. Chem. Phys.* 1990, **92**, 508-517.

45. S. Nosé, *J. Chem. Phys.* 1984, **81**, 511-519.

46. G. Bussi, D. Donadio and M. Parrinello, *J. Chem. Phys.* 2007, **126**, 014101.

47. J.K. Nørskov, J. Rossmeisl, A. Logadottir, L. Lindqvist, J.R. Kitchin, T. Bligaard and H. Jonsson, *J. Phys. Chem. B.* 2004, **108**, 17886-17892.

48. K. Kádas, G. Kern and J. Hafner, *Surf. Sci.* 2000, **454**, 494-497.

49. N. Ooi and J.B. Adams, *Surf. Sci.* 2005, **574**, 269-286.

50. M.-F. Ng, M.K. Teo, K.H. Lim, L. Zhou, M.B. Sullivan and S.-W. Yang, *Diamond and Related Mater*. 2008, **17**, 2048-2053.

51. J. Yamauchi, M. Tsukada, S. Watanabe and O. Sugino, *Phys. Rev. B.* 1996, **54**, 5586.

52. M.-H. Tsai and C. Liu, *Phys. Rev. B*. 2001, **63**, 073305.

53. G. Cappellini, G. Satta, M. Palummo and G. Onida, *Phys. Rev. B.* 2002, **66**, 115412.

54. X. Guo and S. Huang, *Electrochim. Acta.* 2018, **284**, 392-399.

55. K. Kadas, G. Kern and J. Hafner, *Phys. Rev. B*. 1998, **58**, 15636.

56. H.-J. Chun, V. Apaja, A. Clayborne, K. Honkala and J. Greeley, *ACS Catal.* 2017, **7**, 3869-3882.

57. J.-H. Montoya, C. Tsai, A. Vojvodic and J. K. Nørskov, *ChemSusChem*, 2015, 8, 2180-2186.

58. T. E Skúlason, S. Bligaard, F. Gudmundsdóttir, Studt, F. J Rossmeisl, Abild-Pedersen, T. Vegge, H. Jónssonac and J. K. Nøskov, *Phys. Chem. Chem. Phys.*, 2012, **14**, 1235–1245.

59. J. Tafel, Z. *Phys. Chem,. Stoechiom. Verwandtschaftsl.*, 1905, **50**, 641.

60. K. Honkala, A. Hellman, I. N. Remediakis, A. Logadottir, A. Carlsson, S. Dahl, C. H. Christensen and J. K. Nørskov, *Science*, 2005, **307**, 555-558

61. S. Wang, V. Petzold, V. Tripkovic, J. Kleis, J. G. Howalt, E. Skúlason, E. M. Fernandez, B. Hvolbaek, G. Jones, A. Toftelund, H. Falsig, M. Björketun, F. Studt, F. AbildPedersen, J. Rossmeisl, J. K. Nørskov and T. Bligaard, *Phys. Chem. Chem. Phys.*, 2011, **13**, 20760-20765.

62. J. Heyrovsky, *Recl. Trav. Chim. Pays-Bas*, 1927, **46**, 582.

63. A. A. Peterson, F. Abild-Pedersen, F. Studt, J. Rossmeisl and J. K. Nørskov, *Energ. Environ. Sci.*, 2010, **3**, 1311-1315.

64. J. Rossmeisl, Z.-W. Qu, H. Zhu, G.-J. Kroes and J. K. Nørskov, *J. Electroanal. Chem.*, 2007, 607, 83-89.

65. M. Wang, S. Liu, T. Qian, J. Liu, J. Zhou, H. Ji, J. Xiong, J. Zhong and C. Yan, *Nature. Commun.* 2019, **10**, 341.

66. F. Zhou, L. M. Azofra, M. Ali, M. Kar, A. N. Simonov, C. McDonnell-Worth, C. Sun, X. Zhang and D.-R. MacFarlane, *Energy Environ. Sci.*, 2017, **10**, 2516-2520.

67. L. Kou , C. Chen and S. C. Smith, *J. Phys. Chem. Lett.* 2015, **6**, 2794-2805.

68. A. Carvalho, M. Wang, X. Zhu, A. S. Rodin, H. Su and A. H. C. Neto, *Nat. Rev. Mater.,* 2016, **1**, 16061.

69. L. Tao, E. Cinquanta, D. Chiappe, C. Grazianetti, M. Fanciulli, M. Dubey, A. Molle and D. Akinwande, *Nat. Nanotech.,* 2015, **10**, 227.

70. R. A. Doganov, S. P. Koening, Y. Yeo, K. Watanabe, T. Taniguchi and B. Özyilmaz, *Appl. Phys. Lett.* 2015, 106, 083505.

71. V. Tayari, N. Hemsworth, I. Fakih, A. Favron, E. Gaufrès, G. Gervais, R. Martel and T. Szkopek, *Nature. Commun.* 2015, **6**, 7702.

72. J. Na, Y. T. Lee, J. A. Lim, D. K. Hwang, G.-T. Kim, W. K. Choi and Y.-W. Song, *ACS Nano* 2014, **8**, 11753-11762.

73. J.-S. Kim, Y. Liu, W. Zhu, S. Kim, D. Wu, L. Tao, A. Dodabalapur, K. Lai and D. Akinwande, *Sci. Rep.* 2015, **5**, 8989.

74. L. Zhang, L. Ding, X. Yang, and H. Wang, *Angew. Chem. Ed. Int.* 2019, **131**, 2638-2642.

Graphic Abstract